

Facile integration of an Al-rich $Al_{1-x}In_xN$ photodetector on free-standing GaN by radio-frequency magnetron sputtering

Xinke Liu(刘新科), Zhichen Lin(林之晨), Yuheng Lin(林钰恒), Jianjin Chen(陈建金), Ping Zou(邹苹), Jie Zhou(周杰), Bo Li(李博), Longhai Shen(沈龙海), Deliang Zhu(朱德亮), Qiang Liu(刘强), Wenjie Yu(俞文杰), Xiaohua Li(黎晓华), Hong Gu(顾泓), Xinzhong Wang(王新中), and Shuangwu Huang(黄双武)
Citation: Chin. Phys. B, 2023, 32 (**11**): 117701. DOI: 10.1088/1674-1056/acbf25
Journal homepage: http://cpb.iphy.ac.cn; http://iopscience.iop.org/cpb

What follows is a list of articles you may be interested in

Normally-off AlGaN/GaN heterojunction field-effect transistors with *in-situ* AlN gate insulator

Taofei Pu(蒲涛飞), Shuqiang Liu(刘树强), Xiaobo Li(李小波), Ting-Ting Wang(王婷婷), Jiyao Du(都继瑶), Liuan Li(李柳暗), Liang He(何亮), Xinke Liu(刘新科), and Jin-Ping Ao(敖金平)
Chin. Phys. B, 2022, 31 (**12**): 127701. DOI: 10.1088/1674-1056/ac7a0e

Hybrid-anode structure designed for a high-performance quasi-vertical GaN Schottky barrier diode

Qiliang Wang(王启亮), Tingting Wang(王婷婷), Taofei Pu(蒲涛飞), Shaoheng Cheng(成绍恒),Xiaobo Li(李小波), Liuan Li(李柳暗), and Jinping Ao(敖金平)
Chin. Phys. B, 2022, 31 (**5**): 057702. DOI: 10.1088/1674-1056/ac272a

Effect of anode area on the sensing mechanism of vertical GaN Schottky barrier diode temperature sensor

Ji-Yao Du(都继瑶), Xiao-Bo Li(李小波), Tao-Fei Pu(蒲涛飞), and Jin-Ping Ao(敖金平)
Chin. Phys. B, 2022, 31 (**4**): 047701. DOI: 10.1088/1674-1056/ac3223

Band alignment between NiO_x and nonpolar/semipolar GaN planes for selective-area-doped termination structure

Ji-Yao Du(都继瑶), Ji-Yu Zhou(周继禹), Xiao-Bo Li(李小波), Tao-Fei Pu(蒲涛飞), Liu-An Li(李柳暗), Xin-Zhi Liu(刘新智), and Jin-Ping Ao(敖金平)
Chin. Phys. B, 2021, 30 (**6**): 067701. DOI: 10.1088/1674-1056/abdb21

Monolithic epitaxy and optoelectronic properties of single-crystalline γ-In_2Se_3 thin films on mica

Xibo Yin(尹锡波), Yifan Shen(沈逸凡), Chaofan Xu(徐超凡), Jing He(贺靖), Junye Li(李俊烨), Haining Ji(姬海宁), Jianwei Wang(王建伟), Handong Li(李含冬), Xiaohong Zhu(朱小红), Xiaobin Niu(牛晓滨), and Zhiming Wang(王志明)
Chin. Phys. B, 2021, 30 (**1**): 017701. DOI: 10.1088/1674-1056/abcf32

Facile integration of an Al-rich $Al_{1-x}In_xN$ photodetector on free-standing GaN by radio-frequency magnetron sputtering

Xinke Liu(刘新科)[1], Zhichen Lin(林之晨)[1], Yuheng Lin(林钰恒)[1], Jianjin Chen(陈建金)[2], Ping Zou(邹苹)[1], Jie Zhou(周杰)[1], Bo Li(李博)[1], Longhai Shen(沈龙海)[2], Deliang Zhu(朱德亮)[1], Qiang Liu(刘强)[3], Wenjie Yu(俞文杰)[3], Xiaohua Li(黎晓华)[1], Hong Gu(顾泓)[4], Xinzhong Wang(王新中)[5], and Shuangwu Huang(黄双武)[1,†]

[1] *College of Materials Science and Engineering, Institute of Microelectronics (IME), Guangdong Research Center for Interfacial Engineering of Functional Materials, Shenzhen University, Shenzhen* 518060, *China*

[2] *School of Science, Shenyang Ligong University, Shenyang* 110159, *China*

[3] *State Key Laboratory of Functional Materials for Informatics, Shanghai Institute of Microsystem and Information Technology, Chinese Academy of Sciences, Shanghai* 200050, *China*

[4] *Gusu Laboratory of Materials Science, Suzhou* 215123, *China*

[5] *Information Technology Research Institute, Shenzhen Institute of Information Technology, Shenzhen* 518172, *China*

(Received 26 November 2022; revised manuscript received 3 February 2023; accepted manuscript online 27 February 2023)

$Al_{1-x}In_xN$, a III-nitride semiconductor material, is currently of great research interest due to its remarkable physical properties and chemical stability. When the Al and In compositions are tuned, its band-gap energy varies from 0.7 eV to 6.2 eV, which shows great potential for application in photodetectors. Here, we report the fabrication and performance evaluation of integrated $Al_{1-x}In_xN$ on a free-standing GaN substrate through direct radio-frequency magnetron sputtering. The optical properties of $Al_{1-x}In_xN$ will be enhanced by the polarization effect of a heterostructure composed of $Al_{1-x}In_xN$ and other III-nitride materials. An $Al_{1-x}In_xN$/GaN visible-light photodetector was prepared by semiconductor fabrication technologies such as lithography and metal deposition. The highest photoresponsivity achieved was 1.52 $A\cdot W^{-1}$ under 365 nm wavelength illumination and the photodetector was determined to have the composition $Al_{0.75}In_{0.25}N$/GaN. A rise time of 0.55 s was observed after transient analysis of the device. The prepared $Al_{1-x}In_xN$ visible-light photodetector had a low dark current, high photoresponsivity and fast response speed. By promoting a low-cost, simple fabrication method, this study expands the application of ternary alloy $Al_{1-x}In_xN$ visible-light photodetectors in optical communication.

Keywords: $Al_{1-x}In_xN$, photodetector, GaN, radio-frequency magnetron sputtering, ternary alloy

PACS: 77.84.Bw, 07.57.Kp, 71.55.Eq, 81.15.Cd **DOI:** 10.1088/1674-1056/acbf25

1. Introduction

III-nitride semiconductor material has been intensively applied in optoelectronic and electronic devices because of its exceptional physical and chemical properties, especially its excellent photoelectric properties.[1–3] In particular, $Al_{1-x}In_xN$ is considered to be a powerful candidate material for optical and electronic devices. The band gap of $Al_{1-x}In_xN$ can be tuned from 0.7 eV (InN) to 6.2 eV (AlN) by adjusting the Al/In ratio, thereby covering an unprecedented spectral range in the ultraviolet and infrared bands, making it feasible to select a cut-off wavelength for a single-wave segment or multi-wave segment photodetector.[4–6] Extensive research on $Al_{1-x}In_xN$ has been carried out since 2000, but it is difficult to grow, making it the least attractive material among the ternary nitride alloys. The growth process of $Al_{1-x}In_xN$ ternary alloys involves multi-alloy phases of different compositions and structures, and the unintentional doping of nitrogen vacancies can seriously affect the photoresponsivity of any photodetector.[7] Therefore, it is crucial to research the fabrication of high-performance ternary alloy $Al_{1-x}In_xN$ material. To develop a high-performance $Al_{1-x}In_xN$ visible-light photodetector, substrate selection is also essential. A low degree of lattice mismatch between Al-rich $Al_{1-x}In_xN$ and GaN makes it easier to obtain single-phase $Al_{1-x}In_xN$. Theoretically, a two-dimensional electron gas will be generated at the GaN interface in the $Al_{1-x}In_xN$/GaN heterostructure, providing both a high carrier density and high mobility.[8–15] One of the main disadvantages of ternary nitride synthesis is the challenge of solid solution between the binary compounds, i.e., GaN, AlN and InN. The synthesis of $Al_{1-x}In_xN$ alloys using molecular beam epitaxy or metal-organic vapor phase epitaxy requires very high temperatures and there are often phase separation effects. In comparison, radio-frequency magnetron sputtering (RF-MS) permits the preparation of $Al_{1-x}In_xN$ at low temperatures and allows for a non-toxic reaction, mass production and the deposition of single-phase $Al_{1-x}In_xN$ over large areas.[16–18] Currently, an exciting route for fabricating photodetectors is to deposit $Al_{1-x}In_xN$ film on a GaN substrate by RF-MS.[5,19]

In this work, we successfully fabricated an $Al_{1-x}In_xN$/GaN visible-light photodetector by direct RF-MS. The $Al_{1-x}In_xN$/GaN sample was characterized by scanning

†Corresponding author. E-mail: mark_huang@szu.edu.cn

© 2023 Chinese Physical Society and IOP Publishing Ltd

electron microscopy (SEM), x-ray photoelectron spectroscopy (XPS), x-ray diffraction (XRD) and UV–visible spectroscopy to evaluate its chemical composition, crystallinity and optical properties. These represent the quality of the $Al_{1-x}In_xN$ used in the photodetector described in the remainder of this paper. Next, the $Al_{1-x}In_xN$/GaN photodetector was characterized by the *I*–*V* curve, spectral responsivity and response time in order to evaluate the device quality.

2. Experimental details

$Al_{1-x}In_xN$ films were grown directly on a free-standing GaN substrate by RF-MS, and the sputtering target was composed of a sheet of In metal (99.999% purity) attached to the surface of the Al target (99.999% purity). A schematic of the deposition chamber is shown in Fig. 1(a). Firstly, the substrate and Al target were ultrasonically cleaned in anhydrous ethanol for 20 min and blown dry with nitrogen. Then, the substrate and the In/Al target were placed in the deposition system. The reaction chamber has two parallel electrodes: the upper one was assigned as the cathode and substrate support while the lower one was the anode and mounting gear of the In/Al target. The anode is connected to the water-cooling system. Preconditioning of the substrate surface was performed with Ar plasma (DC bias 300 V) at a chamber pressure of 30 Pa for 15 min to activate the surface bonds. Next, the reaction chamber was vacuumed to 5×10^{-4} Pa under 1 Pa chamber pressure and 300 W RF power, and the target was splashed in the argon plasma for 10 min with the aim of removing contaminants. Meanwhile, the chamber pressure was 1 Pa, the Ar:N_2 flow ratio was 60:40, the deposition time was 1 h, the substrate temperature was 350 °C and the distance between the substrate and target was 7 cm. Finally, fork finger electrodes of Ni (20 nm)/Au (50 nm) were prepared on $Al_{1-x}In_xN$/GaN using UV lithography and electron-beam evaporation.

The thickness of the Supra 55 sapphire was measured by SEM. The XRD curve was measured by a D8 Advance to calculate the structures, elements, chemical states and morphologies of the films. XPS spectra were taken by a 220 VG ESCALABi-XL system with a constant energy source of 20 eV, C 1s (284.6 eV) was used for calibration and monochromatic Al $K\alpha$ (1486.6 eV) was the x-ray source. A UV–visible spectrometer (Shimadza-2450, Tokyo, Japan) was used to characterize the absorbance of the films in the range of 300–800 nm. The electrical characteristics of the $Al_{1-x}In_xN$/GaN photodetector were studied with a Keithley 4200-SCS semiconductor parameter analyzer (Keithley, Beaverton, OR, USA). All measurements were carried out at room temperature.

3. Results and discussion

Figure 1(a) shows a schematic diagram of the principle of the $Al_{1-x}In_xN$ film deposition process. The combined probability of targeting Al and In with nitrogen is almost consistent with the sputtering path; the sputtering yield of the target material was changed by designing the ratio of the Al/In target material. Herein we have fabricated Al-rich $Al_{1-x}In_xN$ film. The SEM image in Fig. 1(b) shows a highly compact $Al_{1-x}In_xN$ layer on a thick GaN base layer with a thickness of about 1.04 μm. It can be seen that the grown layer has no cracks and exhibits good adhesion.

The elemental composition and chemical composition of $Al_{1-x}In_xN$ were further understood by XPS analysis. Figures 1(c) and 1(d) show the Al 2p and In $3d_{5/2}$ core-level spectra, respectively. As a binding energy reference, the C 1s peak from contaminating carbon is set at 284.6 eV. The corresponding Al 2p core-level photoelectron spectrum is deconvoluted into two main components at 73.92±0.1 eV and 73.21±0.1 eV, which are assigned to Al–N and Al–Al bonds, respectively. The $In3d_{5/2}$ core-level spectrum of the $Al_{1-x}In_xN$ sample is deconvoluted into three main sub-peaks centered at 444.15±0.1 eV, 444.21±0.1 eV and 445.15±0.1 eV, which are attributed to In–In, In–N and In–O bonds, respectively, with the In–N sub-peak being the most dominant. These results are consistent with previous studies which confirmed the formation of an $Al_{1-x}In_xN$ layer.[20,21] However, the appearance of In–O bonds is possibly due to the formation of a thin oxide layer on the surface of the $Al_{1-x}In_xN$. The Al–Al and In–In bond components are attributed to a higher concentration of active In and Al atoms reaching the growth sites compared with active N atoms at this temperature.[22–24]

Figure 1(e) depicts the XRD pattern of the as-prepared $Al_{1-x}In_xN$, and the observed diffraction peaks correspond to (100), (002) and (102) planes of wurtzite $Al_{1-x}In_xN$. In particular, the phases of Al, In and AlN and InN are not observed, indicating any phase separation in the sample. Based on the position of the (100) and (002) peaks of $Al_{1-x}In_xN$, we can calculate the lattice parameters of the samples. The lattice constants a and c for $Al_{1-x}In_xN$ are determined as 2.83 Å and 5.16 Å, respectively. The crystallite size of $Al_{1-x}In_xN$ is calculated from the (002) peak according to Scherrer's equation, $D = 0.89\lambda/\beta\cos\theta$,[25] and the crystallite size D is 12.52 nm. The alloy composition $Al_{1-x}In_xN$ along the (002) plane is calculated using Vegard's law and Vegard's rule that all growing films are supposed to be pressure-free, as shown below:[7]

$$C_{\mathrm{AlInN}} = (1-x)C_{\mathrm{InN}} + xC_{\mathrm{AlN}}. \tag{1}$$

In Eq. (1), the lattice constants of $Al_{1-x}In_xN$, AlN (4.982 Å) and InN (5.703 Å) are represented by C_{AlInN}, C_{AlN} and C_{InN},

respectively. The result concerning the In content x for $Al_{1-x}In_xN$ is 0.25. Due to the low symmetry of the hexagonal wurtzite crystal structure, the positive and negative ions that deviate from the inside of the crystal produce dipole moments, causing ion polarization. Polarization has an important influence on the photoelectric properties of materials.[26,27] To further investigate the optical properties of $Al_{1-x}In_xN$, the absorbance of $Al_{1-x}In_xN$/GaN heterostructures was measured, as shown in Fig. 1(f). It can be observed that the absorbance of the $Al_{1-x}In_xN$/GaN heterostructures has significantly improved compared with that of $Al_{1-x}In_xN$, which can be attributed to the polarized charges at the interface further strengthening the electron–phonon coupling between $Al_{1-x}In_xN$ and GaN. In addition, the exciton energy generated in $Al_{1-x}In_xN$ is mainly dissipated by the lattice vibration in the adjacent GaN substrate, which leads to a shortened exciton life.[28] Through the polarization effect between $Al_{1-x}In_xN$ and GaN, the energy structure of $Al_{1-x}In_xN$ is adjusted to improve the light absorption capacity. Noticed that the most substantial absorbance peak of $Al_{1-x}In_xN$ emerges at $\sim$ 340 nm in Fig. 1(f). The incident wavelength interval of 300–400 nm has higher absorbance, and two excitation absorption peaks appear. There are no significant absorption peaks above 400 nm for $Al_{1-x}In_xN$/GaN. Therefore, a 365 nm wavelength light source was used in the following device tests. Thus, the absorption rate of $Al_{1-x}In_xN$ can be defined as $\mu = 1 - 1/10^{\theta}$. Note that $\theta = \log_{10}(I_0/I_t)$, where I_0 and I_t are the intensities of the incident and transmitted light, respectively.[29] The apparent optical band-gap energy (E_g) is obtained by linear fitting the squared absorption coefficient as a function of the light quantum in the Tauc plot (in Fig. 1(g)). Light scattering as well as reflection loss are ignored here.[2,19] The equation is[30]

$$ah\nu = C(h\nu - E_g)^m, \tag{2}$$

where C is an energy-independent constant and another constant m is called the power factor of the transition mode $Al_{0.75}In_{0.25}N$. For a direct band-gap semiconductor like $Al_{1-x}In_xN$ alloy $m = 1/2$. Figure 1(g) shows the relationship between the absorption coefficient a and the incident light quantum $h\nu$ of the $Al_{1-x}In_xN$ on GaN. The energy of the optical band gap is calculated according to the absorption spectrum by Tauc's law, and the result is 3.19 eV.[31]

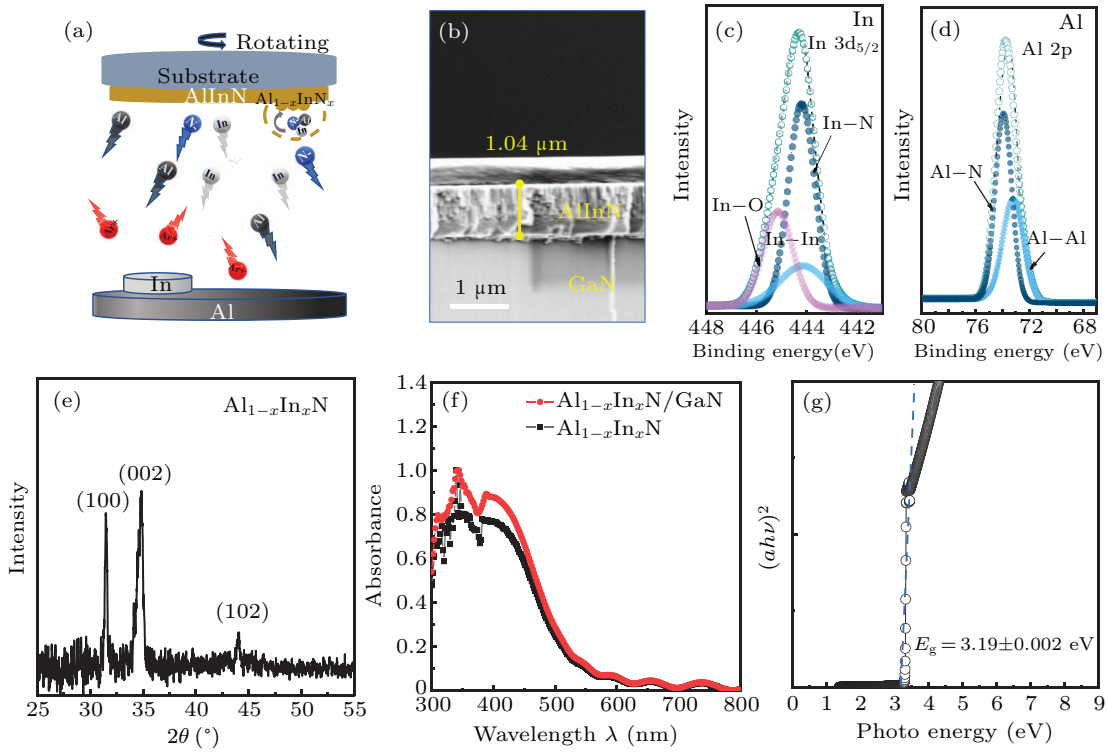


Fig. 1. (a) Schematic diagram of the $Al_{1-x}In_xN$ film deposition process. (b) A cross-sectional SEM image of $Al_{1-x}In_xN$/GaN. XPS spectra of $Al_{1-x}In_xN$ consist of the (c) Al 2p core level and (d) In $3d_{3/2}$ core level. (e) XRD patterns of $Al_{1-x}In_xN$. (f) Optical absorbance spectra of $Al_{1-x}In_xN$/GaN and $Al_{1-x}In_xN$. (g) Tauc plots of $Al_{1-x}In_xN$.

Further energy level alignment characterization of $Al_{0.75}In_{0.25}N$ and GaN was done by XPS combined with energy band theory. XPS has been proven to be an efficient way to determine the band offset at a heterojunction interface.[32,33] In order to determine the valence band offset (VBO) of the $Al_{0.75}In_{0.25}N$/GaN interface, the Al 2p and Ga 2d core-level spectra were employed for the $Al_{0.75}In_{0.25}N$ and GaN materials, respectively. As shown in Figs. 2(a) and 2(b), the following formulae can be used to calculate the VBO ΔE_v and conduction band offset ΔE_c of $Al_{0.75}In_{0.25}N$ and GaN:[34]

$$\Delta E_v = (E_{\text{Al 2p}}^{\text{AlInN}} - E_v^{\text{AlInN}})$$

$$- \left(E_{\text{Ga 3d}}^{\text{GaN}} - E_{\text{v}}^{\text{GaN}}\right) - \Delta E_{\text{CL}}, \tag{3}$$

$$\Delta E_{\text{CL}} = E_{\text{Al 2p}}^{\text{AlInN}} - E_{\text{Ga 3d}}^{\text{GaN}}, \tag{4}$$

$$\Delta E_{\text{c}} = \left(E_{\text{g}}^{\text{AlInN}} - E_{\text{g}}^{\text{GaN}}\right) + \Delta E_{\text{v}}^{\text{AlInN/GaN}}. \tag{5}$$

The vacuum level is taken as the forward reference. Obviously, the $Al_{0.75}In_{0.25}N$/GaN system has a type II alignment in Fig. 2(c). Under UV irradiation, interlayer transitions may occur at the lowest part of the conduction band and the highest part of the valence band and the charge separation of photoinduced carriers can reduce charge recombination, which also indicates that the device may show excellent performance in optoelectronic devices. Therefore, a $Al_{0.75}In_{0.25}N$/GaN photodetector was prepared to demonstrate the ability to detect light.

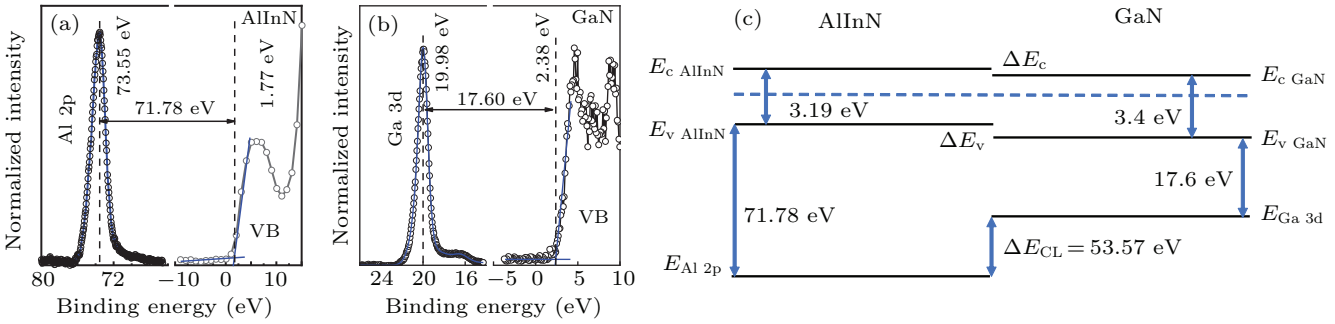


Fig. 2. The core-level and valence band spectra for (a) $Al_{1-x}In_xN$ and (b) bulk GaN samples. (c) Schematic of energy band line-up at the $Al_{1-x}In_xN$/GaN interface.

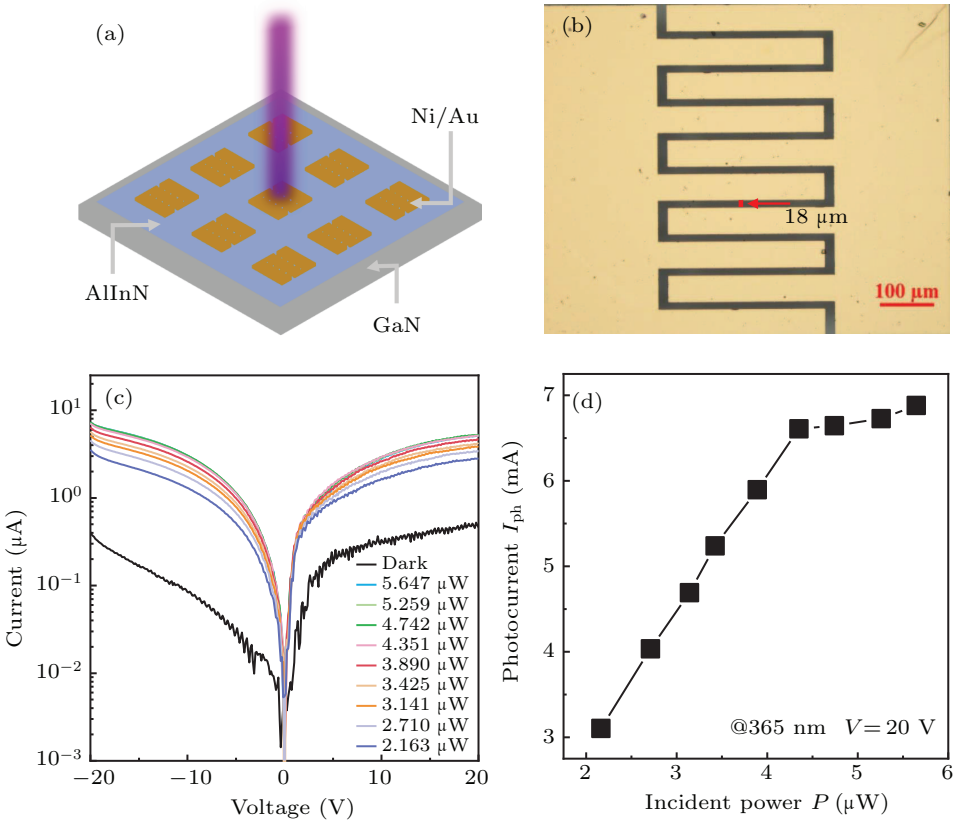


Fig. 3. (a) Three-dimensional schematic structure of the $Al_{1-x}In_xN$ /GaN photodetector. (b) Optical microscopy maps of the individual array devices. (c) The relationship between different incident powers at bright current and dark current and voltage. (d) Photocurrent of the $Al_{1-x}In_xN$/GaN photodetector under different incident powers of a 365 nm laser.

Figure 3(a) shows a three-dimensional schematic view of an $Al_{0.75}In_{0.25}N$ photodetector fabricated on a GaN substrate. Figure 3(b) shows one of the electrodes of the transparent array. The two fork-shaped interdigital contacts consist of Au (50 nm)/Ni (20 nm), the separation of the finger gaps is 18 μm and the effective area is 4.82 μm^2. The current–voltage (I–V) curves of the device at different laser incident powers for a single wavelength of 365 nm are used to further analyze the critical parameters of the photodetector.

The I–V curves of devices with different incident powers and voltages were increased from −20 V to 20 V. The measured I–V curves are shown in Fig. 3(c); it can be observed that I_{light} increases as the power increases. This phenomenon is attributed to the role of photoinduced carriers generated by

the device under laser irradiation. To quantify the photosensitive performance of the photodetector, the photocurrent I_{ph} is defined as[35]

$$I_{ph} = |I_{light}| - |I_{dark}|. \tag{6}$$

In Eq. (6), I_{dark} is the current in dark conditions and I_{light} is the current under light irradiation. Significantly, the device still shows high photocurrent at a low incident power of 2.0163 μW, indicating strong low-light detection capability. Figure 3(d) shows the extracted I_{ph} plotted as a function of the effective power (P) irradiated under a wavelength of 365 nm at a bias voltage of 20 V. The upward trend of I_{ph} slowed down when $P > 4.5$ μW. As reported in previous literature,[36] this phenomenon can be attributed to the light saturation of absorption and the trapping of electrons and holes due to the existence of defects and charge impurities.

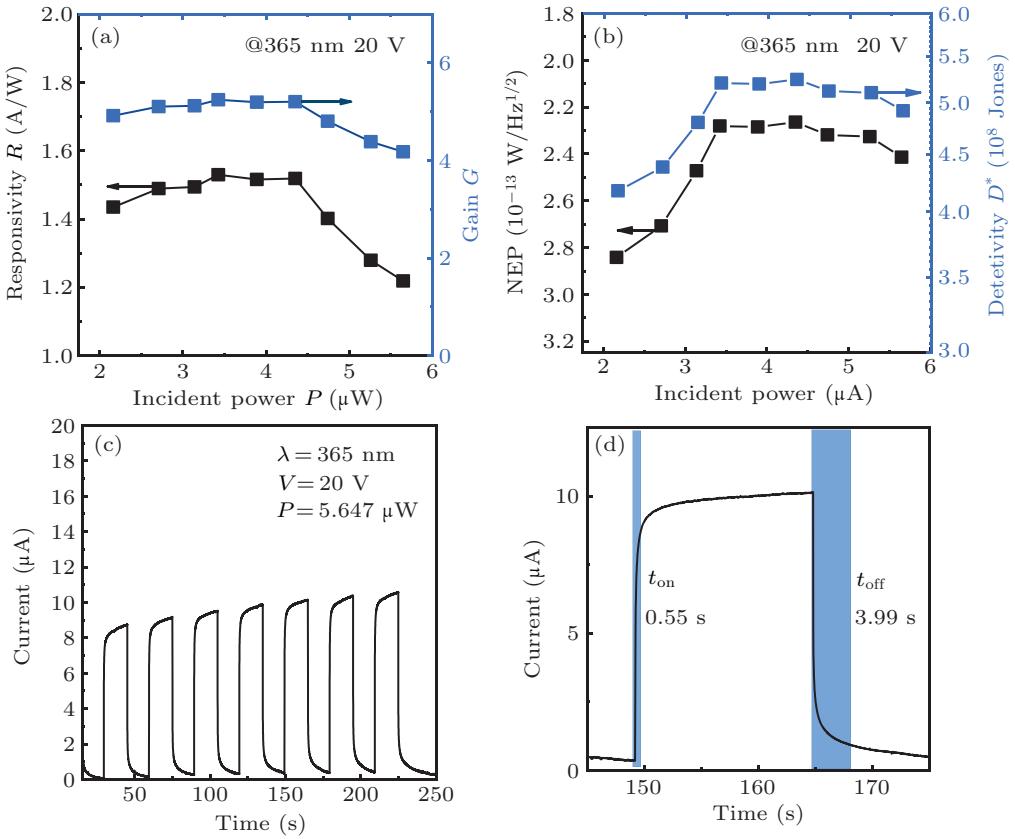


Fig. 4. (a) and (b) Incident power evolution of G, R, NEP and D^* for the $Al_{1-x}In_xN$/GaN photodetector. (c) The switching characteristics of the $Al_{1-x}In_xN$/GaN photodetector under 365 nm illuminations at a voltage of 20 V. (d) The rise time and fall time for the $Al_{1-x}In_xN$ /GaN photodetector.

Figure 4(a) shows the photoresponsivity R and photoconductive gain G of the fabricated device as a function of the effective power at 365 nm wavelength under a bias voltage of 20 V. R is a significant parameter in the performance of photodetectors, and can quantify the spectral and frequency characteristics of photoconversion. R is calculated by[37]

$$R = \frac{|I_{light}| - |I_{dark}|}{S \times P_i}, \tag{7}$$

where I_{ph} is extracted from Eq. (6), S and P_i are the area of active regions of the device and power density of the incident laser irradiation, respectively. The photoconductivity gain G is defined as the number of photogenerated carriers that are generated from unit photons, and is another important parameter for the evaluation of a photodetector. It is calculated by[37]

$$G = \frac{I_{ph}}{P_{abs}} \frac{h\nu}{q}, \tag{8}$$

where P_{abs} is the absorbed power, which is defined as $P_{abs} = \mu P_i$, with μ the absorption percentage calculated above and P_{in} the incident power, h is Plank's constant, ν is the frequency of the incident laser and q is the elementary charge.[42] With increasing incident power, both R and G show a trend of first rising and then decreasing. The $Al_{0.75}In_{0.25}N$/GaN photodetector has the highest responsivity of 1.52 $A \cdot W^{-1}$ at an incident laser power is 3.425 μW, and G also reaches its maximum value at the same power. This phenomenon can be explained by the saturation of the defect state at the interface and the low carrier recombination frequency under a low-power laser as well as the long carrier lifetime.[29] To further discuss the performance of the $Al_{0.75}In_{0.25}N$ photodetector we calculated the noise equivalent power (NEP) and the normalized detection rate (D^*) at different incident powers at a wavelength of 365 nm in Fig. 4(b). The NEP can quantify the detection capability of the photodetector, with a smaller NEP indicating a

higher sensitivity. The NEP can be calculated as follows:[38]

$$\mathrm{NEP} = \frac{(2qI_{\mathrm{dark}}\Delta f)^{1/2}}{R}, \tag{9}$$

where R is obtained from Eq. (7) and Δf is the bandwidth. Usually, the dark current makes the major contribution, and causes scattering noise, Johnson–Nyquist noise and flicker noise. The parameter D^* contributes to quantifying the signal detected by the photodetector. D^* can be calculated as follows:[38]

$$D^* = \frac{A^{1/2}}{\mathrm{NEP}}, \tag{10}$$

where A is the effective area of the $Al_{1-x}In_xN$ under the laser irradiation conditions. The NEP can be extracted from Eq. (10). As shown in Fig. 4(b), the lowest NEP value is 2.26×10^{-13} W·Hz$^{-1/2}$ and the highest D^* value is 9.61×10^{8} Jones calculated for the $Al_{1-x}In_xN$ photodetector at 365 nm laser wavelength and 20 V bias.

Figure 4(c) shows the periodic flow over time of the $Al_{1-x}In_xN$/GaN photodetector under a continuous light pulse. The pulsed light is set to be on or off every 10 s under the 365 nm laser (5.647 μW) and 20 V bias. We can see that the device has a relatively stable switching characteristic. The rise time (t_{rise}) from the dark signal to 90% of the maximum signal upon illumination and the fall time (t_{fall}) to 10% are commonly used to characterize the temporal response of a photodetector. As shown in Fig. 4(d), the calculated t_{rise} and t_{fall} for the $Al_{1-x}In_xN$/GaN photodetector are 0.55 s and 3.99 s, respectively. The $Al_{1-x}In_xN$ photodetector based on a GaN substrate achieves a fast photoresponse, and benefits from the formation of a two-dimensional electron gas at the $Al_{1-x}In_xN$/GaN heterojunction interface and the polarization effect. However, the device shows a long decay time after the optical stimulus has been removed; one of the reasons for this is that $Al_{1-x}In_xN$ is associated with punctate impurities and defects in the substrate.[40] To emphasize the advances achieved with the $Al_{1-x}In_xN$/GaN photodetector a comparison of the results of several studies on the photoresponsivity properties of $Al_{1-x}In_xN$ photodetectors is summarized in Table 1. Compared with other devices, our $Al_{1-x}In_xN$ /GaN device has a higher photoresponsivity and specific detectivity, and the device achieves a fast photoresponse due to the introduction of the GaN substrate.

Table 1. Comparisons of the $Al_{1-x}In_xN$ /GaN photodetector with similar devices.

Photodetector	R (A/W)	Dark current (A)	D^* (Jone)	Response time (s)	Year	Ref.
AlInN/GaN	1.5296	4.09×10^{-7}	9.61×10^{8}	0.55	2022	this work
AlInN/Si	0.47	–	–	–	2018	[41]
AlN/sapphire	0.6×10^{-3}	2.41×10^{-12}	–	0.9	2020	[42]
$Al_{0.33}In_{0.67}N$/glass	1.26×10^{-4}	–	1.2×10^{5}	1.39	2022	[7]
$Al_{0.58}In_{0.42}N$/GaAs	0.06	–	–	0.7	2016	[43]
GaN/sapphire	0.633	–	–	–	2018	[44]

4. Conclusion

In summary, this study has successfully demonstrated an $Al_{1-x}In_xN$/GaN photodetector with low dark current, high photoresponsivity and fast response speed fabricated using the RF-MS deposition method and simple semiconductor fabrication methods. The $Al_{1-x}In_xN$ alloy film was successfully prepared with good crystallinity and homogeneity measured by SEM and XPS core-level spectra. The alloy composition of $Al_{1-x}In_xN$ was then analyzed by XRD, and $x = 0.25$ was calculated. Calculation of the absorbance of the film gave the band gap of $Al_{0.75}In_{0.25}N$ as about 3.19 eV. In addition, the polarization effect of the III-nitride heterostructure has a positive impact on improving the absorption capacity of $Al_{1-x}In_xN$. The electron transport behavior of the $Al_{1-x}In_xN$/GaN heterojunction was further proved by XPS valence band spectroscopy. Subsequently, a $Al_{0.75}In_{0.25}N$ photodetector was prepared, showing excellent performance with a maximum photoresponsivity of 1.52 A·W^{-1} and time to reach maximum photocurrent of 0.55 s under 365 nm laser illumination. Table 1 compared various photodetectors with the one reported in this work. In recent years there have been few reports on $Al_{1-x}In_xN$ alloy, and we have achieved unprecedented performance by controllable fabrication of $Al_{1-x}In_xN$ via physical vapor deposition technology to fabricate a photodetector on GaN substrate.

Acknowledgements

Project supported by the National Natural Science Foundation of China (Grant Nos. 61974144, 62004127, and 12074263), Key-Area Research and Development Program of Guangdong Province (Grant Nos. 2020B010174003 and 2020B010169001), Guangdong Science Foundation for Distinguished Young Scholars (Grant No. 2022B1515020073), the Science and Technology Foundation of Shenzhen (Grant No. JSGG20191129114216474), and the Open Project of State Key Laboratory of Functional Materials for Informatics.

References

[1] Zawadzka A M, Karakas A, Plóciennik P and Szatkowski J, Łukasiak Z, Kapceoglu A, Ceylan Y and Sahraoui B 2015 *Dyes and Pigments*

112 116
[2] Yamaguchi S, Kariya M, Nitta S, Kato H, Takeuchi T, Wetzel C, Amano H and Akasaki I 1998 *Journal of Crystal Growth* **195** 309
[3] Lobanova A V, Segal A S, Yakovlev E V and Talalaev R A 2012 *Journal of Crystal Growth* **352** 199
[4] Wang F, Li S F, Sun Q and Jia Y 2010 *Solid State Sciences* **12** 1641
[5] Blasco R, Naranjo F B and Valdueza-Felip S 2020 *Current Applied Physics* **20** 1244
[6] Blasco R, Valdueza-Felip S, Montero D, Sun M, Olea J and Naranjo F B 2020 *Physica Status Solidi (b)* **257** 1900575
[7] Chen J J, Shen L S, Qi D L, Wu L J, Li X, Song J Y and Zhang X L 2022 *Ceramics International* **48** 2802
[8] Carlin J F and Ilegems M 2003 *Appl. Phys. Lett.* **83** 668
[9] Borovac D, Sun W C, Song R, Wierer J J and Tansu N 2020 *Journal of Crystal Growth* **533** 125469
[10] Tan C K, Sun W, Borovac D and Tansu N 2016 *Sci. Rep.* **6** 22983
[11] Velpula R T, Jain B, Philip M R, Nguyen H D, Wang R and Nguyen H P T 2020 *Sci. Rep.* **10** 2547
[12] Laskar M R, Ganguli T, Rahman A A, Arora A, Hatui N, Gokhale M R, Ghosh S and Bhattacharya A 2011 *Appl. Phys. Lett.* **98** 181108
[13] Lupu A, Julien F H, Golka S, Pozzovivo G, Strasser G, Baumann E, Giorgetta F, Hofstetter D, Nicolay S, Mosca M, Feltin E, Carlin J F and Grandjean N 2008 *IEEE Photonics Technology Letters* **20** 102
[14] Edmunds C, Tang L, Li D, Cervantes M, Gardner G, Paskova T, Manfra M J and Malis O 2012 *Journal of Electronic Materials* **41** 881
[15] Jeganathan K, Shimizu M, Okumura H, Yano Y and Akutsu N 2007 *Journal of Crystal Growth* **304** 342
[16] Liu H F, Tan C C, Dalapati G K and Chi D Z 2012 *J. Appl. Phys.* **112** 063114
[17] Cascajero A N, Lerma L M, Felip S V, Navío C, Monroy E, Herráez G M and Naranjo F B 2016 *Jpn. J. Appl. Phys.* **55** 065101
[18] Dong C J, Xu M, Chen Q Y, Liu F S, Zhou H P, Wei Y and Ji H X 2009 *J. Alloys Compd.* **479** 812
[19] Cascajero A N, Felip S V, Lerma L M, Monroy E, Shaw E T, Martin R W, Herráez M G and Naranjo F B 2017 *J. Phys. D: Appl. Phys.* **50** 065101
[20] Lebedev V, Morales F M, Cimalla V, Lozano J G, González D, Himmerlich M, Krischok S, Schaefer J A and Ambacher O 2006 *Superlattices and Microstructures* **40** 289
[21] You Y, Ito A, Tu R and Goto T 2013 *Surface and Coatings Technology* **232** 1
[22] Alizadeh M, Goh B T, Pandey A K, Dee C F and Rahman S A 2017 *Materials Chemistry and Physics* **199** 408
[23] Alizadeh M, Ganesh V, Mehdipour H, Nazarudin N F F, Goh B T, Shuhaimi A and Rahman S A 2015 *J. Alloys Compd.* **632** 741
[24] Alizadeh M, Mehdipour H, Ganesh V, Ameera A N, Goh B T, Shuhaimi A and Rahman S A 2014 *Appl. Phys. A* **117** 2217
[25] Abed C, Fernandez S, Aouida S, Elhouichet H, Priego F, Castro Y, Mancebo M B G and Munuera C 2020 *Materials (Basel)* **13** 9
[26] Huang Y, Chen D J, Lu H, Shi H B, Han P, Zhang R and Zheng Y D 2010 *Appl. Phys. Lett.* **96** 243503
[27] Heikman S, Keller S, Wu Y, Speck J S, DenBaars S P and Mishra U K 2003 *J. Appl. Phys.* **93** 10114
[28] Edmunds C, Tang L, Cervantes M, Shirazi-Hd M, Shao J, Grier A, Valavanis A, Cooper J D, Li D, Gardner G, Zakharov D N, Ikonić Z, Indjin D, Harrison P, Manfra M J and Malis O 2013 *Phys. Rev. B* **88** 235306
[29] Li Z W, Wu J, Wang C, Zhang H, Yu W J, Lu Y M and Xinke Liu 2020 *Nanophotonics* **9** 1981
[30] Cramer R C, Kyle E C H and Speck J S 2019 *J. Appl. Phys.* **126** 035703
[31] Yeh T S, Wu J H and Lan W H 2008 *Journal of Crystal Growth* **310** 5308
[32] Liu X K, He J Z, Liu Q, Tang D, Jia F, Wen J, Lu T MM, Yu W J, Zhu D L, Liu W J, Cao P J, Han S, Pan J S, He Z B and Ang K W 2015 *Appl. Phys. Lett.* **107** 101601
[33] Li K L, Li Z W, Hong Y H, Hu C, Mao W and Liu X K 2018 *Appl. Phys. Lett.* **113** 143506
[34] Liu X K, Hu C, Li K, Wang W, Li Z W, Ao J, Wu J, He W, Mao W, Liu Q, Yu W and Chung R J 2018 *Nanoscale Res. Lett.* **13** 405
[35] Liu X K, Luo J L, Zhu D L, Lu Y M, Li X L, He J L, Chiu H C, Xu K, Yu W J and Chung R J 2021 *ACS Applied Electronic Materials* **3** 1988
[36] Lähnemann J, Hertog M D, Hille P, Mata M D L, Fournier T, Schörmann J, Arbiol J, Eickhoff M and Monroy E 2016 *Nano Lett.* **16** 3260
[37] Xiao Y F, Min L, Liu X K, Liu W J, Younis U, Peng T H, Kang X W, Wu X H, Shijin Ding and Zhang D W 2020 *Nanophotonics* **9** 3035
[38] Hu S Q, Liao Z L, He J L, Yu W J, Song L J, Wang Q, Li X H and Liu X K 2021 *J. Appl. Phys.* **129** 183106
[39] Weng W Y, Chang S J, Lai W C, Hsueh T J, Shei S C, Zeng X F, Wu S L and Hung S C 2009 *IEEE Photonics Technology Letters* **21** 504
[40] Wu Y C, Liu C H, Chen S Y, Shih F Y, Ho P H, Chen C W, Liang C T and Wang W H 2015 *Sci. Rep.* **5** 11472
[41] Blasco R, Cascajero A N, Rodríguez M J, Montero D, Grenet L, Olea J, Naranjo F B and Felip S V 2018 *Physica Status Solidi (a)* **216** 1800494
[42] Kaushik S, Naik T R, Alka A, Garg M, Tak B R, Ravikanth M, Rao V R and Singh R 2020 *ACS Applied Electronic Materials* **2** 739
[43] Afzal N, Devarajan M and Ibrahim K 2016 *Materials Research Express* **3** 085904
[44] Jain S K, Krishna S, Aggarwal N, Kumar R, Gundimeda A, Husale S C, Gupta V and Gupta G 2018 *Journal of Electronic Materials* **47** 6086